Key Points:
- A finite difference time domain (FDTD) model is used to simulate radar observations of meteors
- Meteor mass estimations are made by combining observed radar cross sections with FDTD simulation results
- A data set of coincident observations by two radar systems is used to verify the mass estimation procedure

Correspondence to:
L. K. Tarnecki,
liane.tarnecki@colorado.edu

Meteoroid Mass Estimation Based on Single-Frequency Radar Cross Section Measurements

L. K. Tarnecki[1] , R. A. Marshall[1] , G. Stober[2], and J. Kero[3]

[1]Smead Aerospace Engineering Sciences, University of Colorado Boulder, Boulder, CO, USA, [2]Institute of Applied Physics & Oeschger Center for Climate Change Research, Microwave Physics, University of Bern, Bern, Switzerland, [3]Swedish Institute of Space Physics (IRF), Kiruna, Sweden

Abstract Both high-power large aperture radars and smaller meteor radars readily observe the dense head plasma produced as a meteoroid ablates. However, determining the mass of such meteors based on the information returned by the radar is challenging. We present a new method for deriving meteor masses from single-frequency radar measurements, using a physics-based plasma model and finite-difference time-domain (FDTD) simulations. The head plasma model derived in Dimant and Oppenheim (2017), https://doi.org/10.1002/2017ja023963 depends on the meteoroids altitude, speed, and size. We use FDTD simulations of a radar pulse interacting with such head plasmas to determine the radar cross section (RCS) that a radar system would observe for a meteor with a given set of physical properties. By performing simulations over the observed parameter space, we construct tables relating meteor size, velocity, and altitude to RCS. We then use these tables to map a set of observations from the MAARSY radar (53.5 MHz) to fully defined plasma distributions, from which masses are calculated. To validate these results, we repeat the analysis using observations of the same meteors by the EISCAT radar (929 MHz). The resulting masses are strongly linearly correlated; however, the masses derived from EISCAT measurements are on average 1.33 times larger than those derived from MAARSY measurements. Since this method does not require dual-frequency measurements for mass determination, only validation, it can be applied in the future to observations made by many single-frequency radar systems.

Plain Language Summary The material left behind as meteoroids burn up in the upper atmosphere has significant effects on atmospheric chemistry and dynamics. However, the amount of mass deposited by any single meteoroid, and therefore the overall input rate, is difficult to calculate. We present a new method for determining individual meteor masses using radar observations and numerical simulations. We use a physics-based model of the meteor plasma distribution to simulate the interaction between a radar pulse and a meteor, and calculate observable quantities. Using these simulations, we relate the radar observations to physical characteristics of the meteor, which we then use to estimate the mass. Since this method only requires a single radar observation to calculate a meteor's mass, we apply it to a set of meteors observed at the same time by two radar systems, and compare the results.

1. Introduction

As a meteoroid travels through an atmosphere it undergoes a process called ablation in which its outer layers are converted into a plasma, primarily due to frictional heating and sputtering. The vast majority of meteoroids that enter the atmosphere are extremely small, on the order of mg to μg (Flynn, 2002), and most of them ablate entirely. Most meteoroids ablate between 80 and 120 km altitude (Ceplecha et al., 1998; Janches et al., 2015; Kero et al., 2012; Schult et al., 2017). Metallic ions originating from the meteoroid itself deposited in this region interact with the existing E-region ionospheric plasma population in various ways. The input of meteoric material can cause the formation of metal layers, change ionospheric conductivities, densities, and compositions, and seed the formation of high-altitude clouds (Ellyett & Kennewell, 1980; Plane, 1991; Rosinski & Pierrard, 1964). However, the mass of any single meteoroid, and therefore the amount of mass it deposits in the atmosphere during ablation, is difficult to determine with sufficient precision. As a result the total meteoric mass flux is poorly constrained, with estimates ranging from 5 to more than 250 tons per day (Plane, 2012). Each estimate depends on the method of observation, the process used to determine individual masses, and the assumed size and velocity distribution of the meteoroid population. Each step incorporates numerous assumptions about the physical processes involved. Additionally,

meteoroids occur in an extremely broad range of sizes, and no single technique can observe the entire distribution. For example, meteor radars readily observe small particles over a large range of masses, ng-mg, while optical camera networks can only detect particles on the order of a mg or larger (Janches et al., 2014; ReVelle, 2003; Schult et al., 2017, 2020; Stober et al., 2011). Optical observations thus neglect the numerous μg-sized meteoroids, while the statistical occurrence of larger meteoroids in radar meteor data is low compared to the occurrence of small and moderately sized particles. Other techniques measure mass more directly, such as analysis of cratering on satellite-based detectors, but have selection biases based on the velocity of incoming particles (Love & Brownlee, 1993). Hunt et al. (2004) showed that high-gain radars also have a velocity bias, and preferentially detect large, fast meteoroids.

The plasma that makes up a meteor consists of two parts: the dense plasma that forms around the meteoroid as it ablates, called the head plasma, and the diffuse plasma left behind, called the trail. High-power large aperture radar systems readily detect the head plasma of meteors, and have been used to do so for decades (McKinley & Millman, 1949). Radar cannot detect the plasma density directly, but instead measure the radar cross section (RCS). The observed RCS depends on the shape, physical extent, and density of the meteor plasma distribution, as well as its location within the radar beam and the radar frequency. Various techniques can also be used to measure the meteor's velocity and spatial location (Elford et al., 1995; Mazur et al., 2020; Steel & Elford, 1991). In this work, we will address the difficulty of converting radar observations of head plasmas into mass estimates and introduce a method that uses results from computer simulations to determine individual masses.

Meteor masses can be inferred from observations ("mass inversion") using various techniques, though the reliability of any given method is difficult to ascertain. Radar mass inversion techniques rely on determining the relationship between observable parameters (primarily RCS, velocity, altitude) and the meteor mass. In general, this requires assumptions about the shape of the head plasma and the physical relationships between the observable parameters and electron density in the head plasma. Close et al. (2004) demonstrates a mass inversion method that relates the size of a meteor to its velocity and altitude, then applies a spherical scattering model to convert between RCS and plasma density.

The simulation method used in this work is based on the method introduced in Marshall and Close (2015). Marshall and Close used a finite difference time domain (FDTD) model to simulate the interaction between an incident radar wave and the head plasma of a meteor, then calculated the RCS that radar systems with various transmission frequencies would observe for a meteor of given size and shape parameters. The FDTD method is discussed in greater detail in Section 3.1.

Marshall and Close (2015) used a simple, spherically symmetric 3D Gaussian model to describe the meteor head plasma. Since this model has two free parameters (variance and peak density) and only a single measurement (RCS), dual-frequency observations are required to uniquely determine the mass. In this work, we incorporate a physics-based model for the meteor head plasma. This model uses radar-measurable parameters including velocity and altitude to define the distribution, requiring fewer assumptions about the structure of the plasma and allowing masses to be derived from a single radar measurement, instead of the dual-frequency method described in Marshall and Close. This plasma model incorporates a more physical description of the meteor plasma, and allows the mass inversion scheme to be applied to any single-frequency set of radar observations, rather than requiring dual-frequency observations. To test and validate this new approach, we apply our method to a set of dual-radar meteor observations, described in the following section. The dual-frequency observations allow the method to be independently validated using coincident meteor observations.

2. Data

The radar data used in this work consists of 485 meteors that were observed coincidentally by MAARSY (53.5 MHz) and EISCAT (929 MHz) radars in Norway between September 30, 2016 and March 25, 2017. Figure 1 shows histograms of the observed RCS values for both radars. In general, the MAARSY RCS values are higher than the EISCAT values by an average of 16.7 dB. EISCAT has a narrow beam width (0.7° HPBW) compared to MAARSY (3.6° HPBW), so most meteors are observed for a longer period with MAARSY than with EISCAT. The narrow beam also restricts the altitudes at which both radars can observe a meteor at the
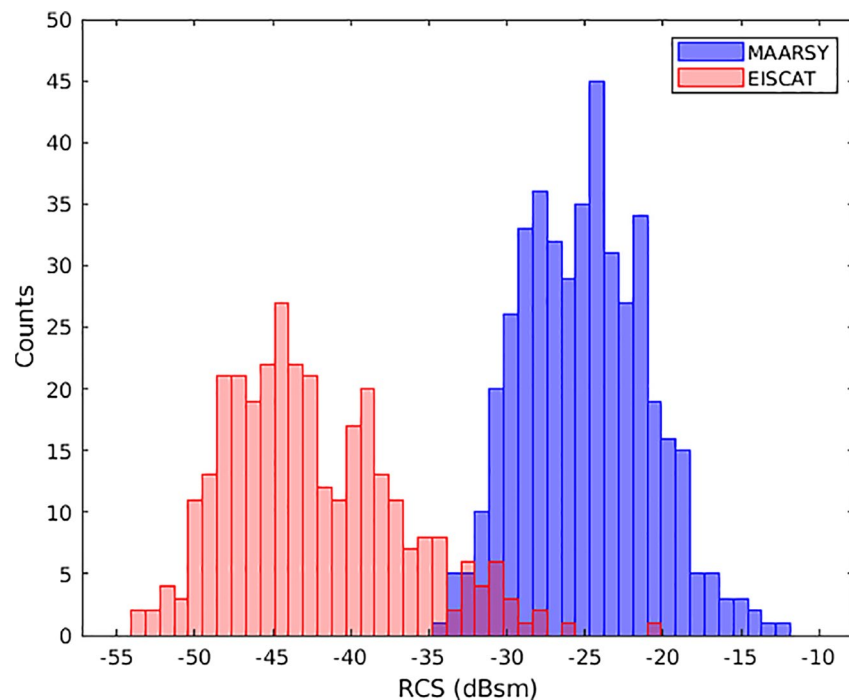
Figure 1. Histograms of the median radar cross section for each radar profile for MAARSY (blue) and EISCAT (red).

same time to a limited range (90–110 km). The data set and observation techniques are described in detail in Schult et al. (2021).

Figure 2 shows three example radar profiles of RCS versus time for observed meteors. The dotted lines indicate the coincident region, during which both radars observed the meteor at the same time. Panel (a) shows a smooth, well-behaved observation. Panel (b) shows a case with some large spikes in the EISCAT observation. Panel (c) shows a case with significant gaps in the MAARSY observation, and in which the coincident region consists of only a few observation points. While we attempt to estimate a mass for every observation, cases such as those in panels (b and c) can lead to unreliable estimates or fall outside of the simulated parameter space. In the case of gaps in the data, we use a linear interpolation to fill in the missing points.

The spikes in the EISCAT data are formed when the meteor target passes a minimum in the narrow EISCAT UHF antenna radiation pattern. There, the antenna gain changes fast as a function of position and the true gain of the antenna differs from the ideal radiation pattern of a Cassegrain antenna used to convert the measured SNR to RCS (see Kero, Szasz, Pellinen-Wannberg, et al., 2008). A mitigation method to avoid these spikes might be to replace RCS values where the antenna gain is lower than a certain threshold with a linear interpolation, as in the case of missing data points. However, testing has shown that the mass estimates for profiles with such artefacts are similarly distributed to those for smooth profiles, and do not produce higher than expected masses. While one might expect that a large artificial spike in RCS would correspond to an increase in the estimated mass, in such cases the data is unphysical and falls outside of the parameter space of the analysis (described in the following section), and thus does not contribute to the mass estimate. In this case, we choose to use the original RCS profiles without replacing any of the data, as doing so does not seem to introduce any bias or artificial inflation to the mass estimates.

3. Methodology

The mass inversion method presented in this work requires FDTD simulations to relate observed RCS profiles to physical plasma distributions. In this section, we describe the FDTD model, the steps of the mass inversion scheme, and the treatment of uncertainty.
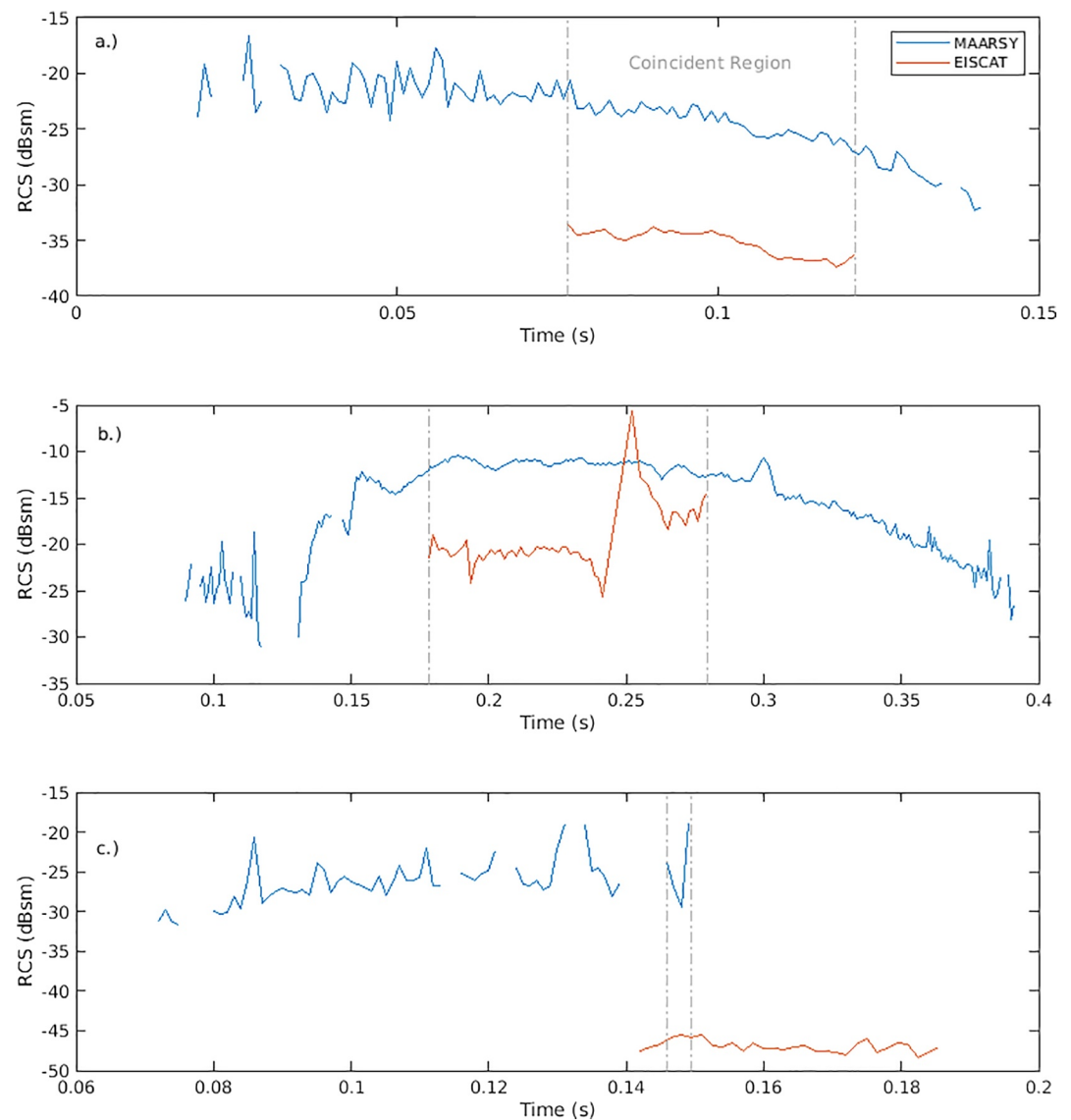
Figure 2. Example radar cross section profiles. The coincident region, where both radar observe the meteor at the same time, is marked by dashed lines. Many profiles are smooth (a), but some have sudden large spikes or troughs (b), significant gaps in the observation, or are only observed coincidentally at a few points (c).

3.1. FDTD Model

The FDTD simulations in this work are based on those in Marshall and Close (2015), which describes the method in detail. The model simulates a radar pulse encountering and scattering from a static plasma distribution. As the total length of a single simulation is on the order of a few microseconds, it is reasonable to assume that the meteor plasma is stationary for the duration of a single radar pulse. The model solves Maxwell's equations in a cold, collisional, magnetized plasma, according to the standard FDTD algorithm presented in Yee (1966). The RCS is estimated using a total-field/scattered-field method near the meteor (within the simulation box), which is mapped to the far field using a near-to-far-field transformation (Inan & Marshall, 2011). Figure 3 shows a sequence of stills from a simulation, showing the radar pulse before encountering the meteor plasma (left) and during and after the scattering of the pulse from the plasma.

Marshall and Close used this method to simulate observations at several frequencies of meteors of various sizes with a 3D Gaussian distribution of plasma density. The meteors were defined by a peak density and a size scale parameter, leading to a system with two unknowns and one measurement (RCS). They suggest
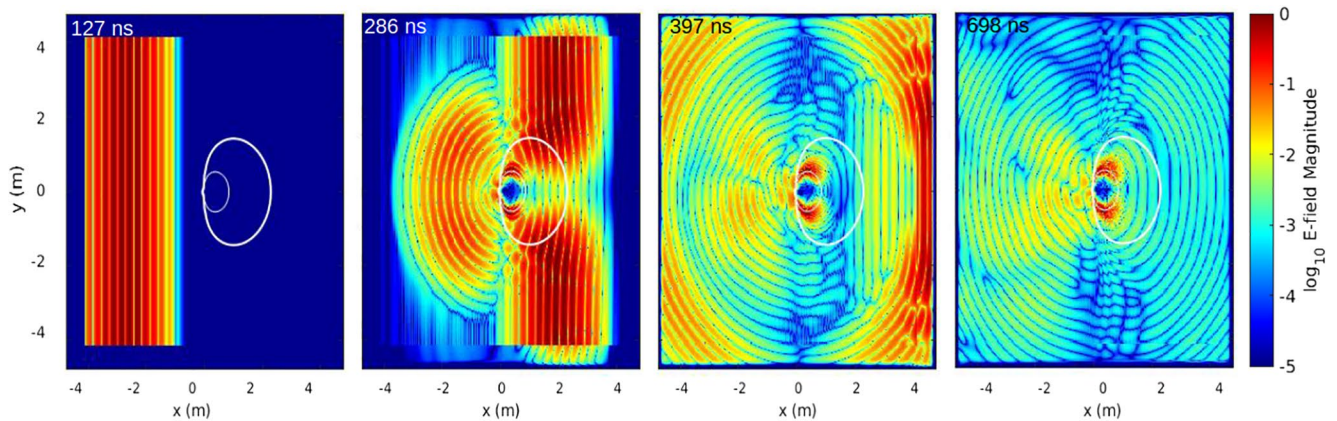
Figure 3. Snapshots from an finite difference time domain simulation. The simulated radar pulse enters the box from the left (panel 1) and interacts with the meteor plasma, represented by the white contour lines (panel 2). The thin inner line represents the overdense area, or the region in which the plasma frequency ω_p is greater than the transmitted frequency ω ($\omega_p \geq \omega$). The thick outer line represents the region in which the plasma frequency has dropped to a factor of e less than the transmitted frequency, ($\omega_p \geq \omega/e$). Some portion of the pulse reflects from the plasma (panel 3), leaving small-scale perturbations behind (panel 4).

that the solution is to combine two simultaneous observations of the same meteor at different frequencies. By implementing a different plasma distribution, we avoid this problem, and can estimate the meteoroid mass using a single frequency observation.

Dimant and Oppenheim (2017) presented a new model for the head plasma of a meteor derived using kinetic theory. The model is built from a first-principles analysis of the plasma formed around a small meteoroid as it travels through an atmosphere, and describes the head plasma at a single instant in time. The density falls off from a peak around the source location roughly exponentially ahead of the meteor, as $1/r^2$ behind it, and as $1/r^3$ perpendicular to the path. Figure 4a shows an example of the Dimant-Oppenheim (DO hereafter) distribution, with relevant density contours. The distribution is fully defined by four parameters: the source meteoroid's radius (r_M), altitude (h), and velocity (U), as well as a plasma density parameter (n_0). The radius and density parameters appear together as a coefficient $n_0 r_M^2$ which cannot be separated in the following analysis, so we treat the product as a single size parameter. Crucially, this allows us to uniquely
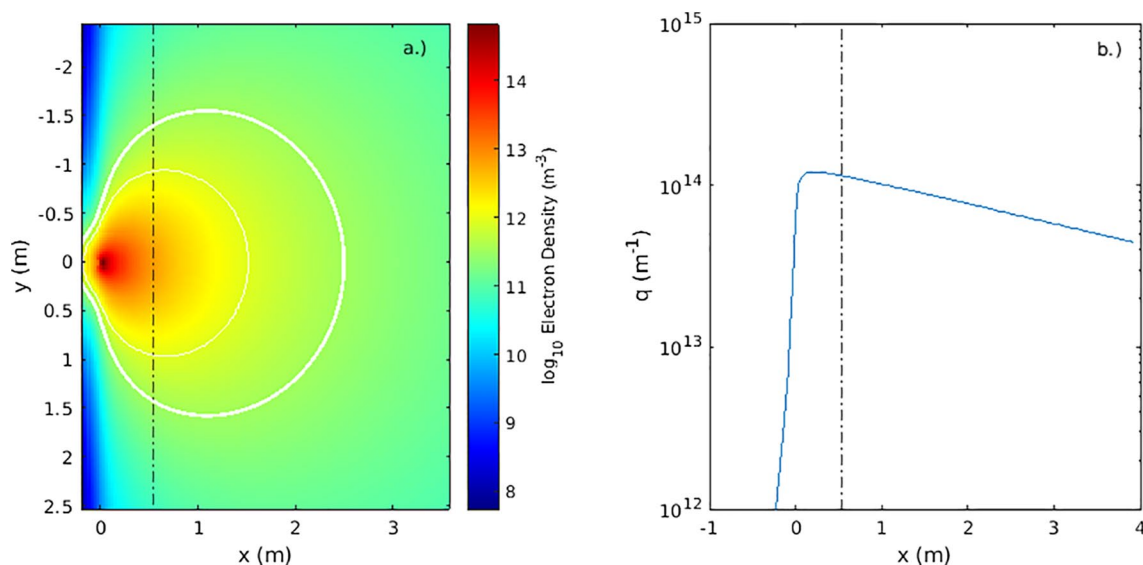

Figure 4. Example of the Dimant-Oppenheim head plasma distribution, for a meteor at 100 km traveling at 60 km/s (a.). Contours are the same as in Figure 3. The location in the tail at which the line density q is calculated is shown by the black dashed line. The value of q at each grid location is shown on the right (b.).
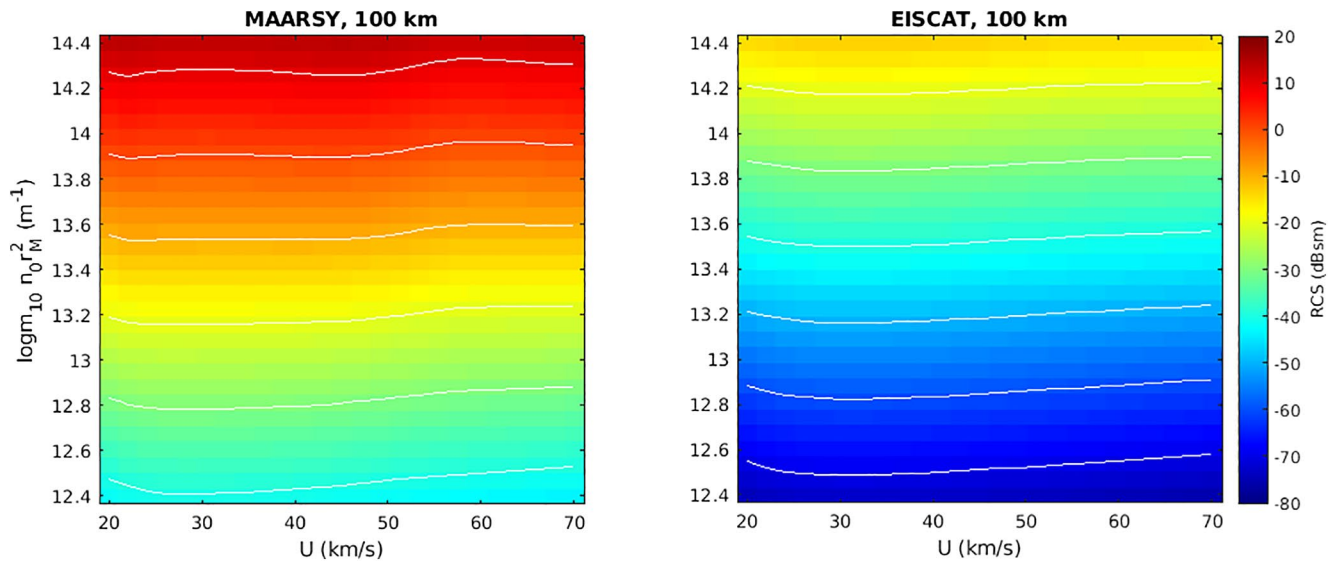
Figure 5. MAARSY (left) and EISCAT (right) lookup tables at 100 km. Contours are drawn at intervals of 10 dB.

define a plasma distribution in terms of three variables, two of which (velocity and altitude) are directly measurable with a radar. By adopting this plasma distribution we have moved from a problem with two unknowns and one measurement to one with three unknowns ($n_0 r_M^2$, h, and U) and three measurements (RCS, h, and U), a solvable system.

By fully defining the plasma distribution, the line density q can be calculated directly. The line density can be thought of as the amount of ionization produced by the meteoroid per unit length along its trajectory. q can thus be calculated by integrating the plasma density in a plane slice through a meteor's tail. This integration is numeric, not analytic, and has some variation depending on the exact location selected (Figure 4b).

In the following analysis, we use data from simulations at four altitudes (95–110 km, with 5 km resolution). At each altitude and for each radar, 750 unique meteors were simulated spanning 25 velocities (20–70 km/s, with 2 km/s resolution), and 30 size parameters ($n_0 r_M^2 = 10^{12.4} - 10^{14.4}$ m^{-1}, uniformly separated in log space). The altitude and velocity parameter ranges were chosen based on the physical occurrence of meteors; the size parameter range was chosen such that the simulated RCS values cover the range of observed values. The general trends in RCS with each parameter are as follows: strong linear increase in RCS (dB) with logarithmically increasing size parameter; weak, approximately linear decrease in RCS with linearly increasing altitude; and weak RCS dependence on velocity, with a peak in RCS around 25 km/s. Figure 5 shows the 100 km altitude lookup tables for each radar system. Note that for any given set of parameters, the FDTD model predicts that MAARSY will observe an RCS that is 20–30 dB greater than EISCAT observes, a difference that is similar but somewhat larger than that observed in the MAARSY/EISCAT coincident data set described in Section 2.

3.2. Mass Inversion Scheme

Once the lookup tables have been created, they are used to invert radar observations to estimate masses. For each time step within a single observation, the scheme is:

1. Use the appropriate lookup table to determine the size parameter $n_0 r_M^2$ from the observed altitude, velocity, and RCS.
2. At each timestep, the DO distribution is now fully defined by the observed altitude, observed velocity, and inferred size parameter. Generate this full head plasma distribution and use it to calculate the line density q.

3. Use q to calculate the mass loss rate ($\frac{dm}{dt} = \frac{qU\mu}{\beta}$) and integrate over the full observation to estimate the mass m.

The lookup tables are defined for a discrete parameter space. In the (likely) event that the observed parameters do not exactly equal the simulated parameters, we linearly interpolate the tables to the observed values. First, the two tables nearest in altitude to the observation are used to interpolate to the observed altitude. Next, this table is interpolated to the observed velocity. Finally, a linear fit in log-log space is applied to the resulting data (RCS as a function of $n_0 r_M^2$) and inverted to estimate the size parameter. This estimate, together with the observed altitude and velocity, constitute the assumed plasma distribution of the meteor at the observation timestep.

The spacing of the simulated data was chosen to limit the error introduced by this linear interpolation, such that this error is small compared to other sources of uncertainty, described later. An exception to this claim is when the observed RCS falls within the Mie scattering regime. At large values of the size parameter, the meteors enter the Mie scattering regime at MAARSY's frequency of 53 MHz. In this case, the relationship between RCS and meteor size is non-linear, and a unique inversion does not exist. While few of the observed meteors appear to fall within this regime, the linear fit can lead to over- or under-estimations of mass for large meteors. This is not an issue for the EISCAT simulations, as at all simulated sizes the meteors are within the Rayleigh scattering regime.

Once the distribution is defined, the line density q is calculated numerically by integrating the density in a slice through the region in the wake of the meteor.

This process is repeated at each timestep in the observation, building an array of q as a function of time. The line density is related to the total mass lost by the meteor at a single moment (dm/dt) by the velocity U, species mass μ, and the ionization efficiency β. The total mass estimate is defined by the integral (Close et al., 2004):

$$m = \int_{t_1}^{t_2} \frac{qU\mu}{\beta} dt \tag{1}$$

In the following analysis, we assume a species mass of $\mu = 5.12 \times 10^{-26}$ kg, based on a composition of 70% oxygen and 30% silicon, and corresponding to a mass density of 700 kg/m^3. We also assume the ionization efficiency profile for iron derived in DeLuca et al. (2018), $\beta = 2.49 \times 10^{-4} U[\text{km/s}]^{2.04}$. This profile is the result of laboratory experiments. While the assumed composition in this work does not include iron, we have adopted the DeLuca et al. (2018) result on the assumption that this velocity-dependent model improves on the assumption of a constant ionization efficiency for all meteors at all speeds, and there are no documented β measurements for oxygen/silicon. The implications of these assumptions are discussed in Section 5.

The bounds of integration are chosen based on the desired mass product. For the purpose of comparison between MAARSY and EISCAT only the mass lost in the coincident region (the "coincident mass") should be considered, so the integral is taken only over the time that both radar observe the meteor. To determine the total mass ablated in the radar beam volume, the integral is taken over the entire observation. Note that any ablation that occurs outside of the radar beam cannot be accounted for.

3.3. Sources of Uncertainty in Modeling and Fitting

The choice of numerical parameters in the FDTD simulation space leads to numerical errors and uncertainty in the estimated RCS values. To quantify these errors, we have run extensive test simulations over simulation parameters and estimated the variation of the resulting RCS. Capturing the relevant physics requires both that the meteor plasma fit entirely within the simulation box, and that the grid size is small enough to resolve both the radar wavelength and the plasma distribution. As the radar pulse enters the dense head plasma the wavelength shrinks, compounding this problem. Even when the grid size is sufficiently small to resolve the geometry of the meteor, there is some variation in the calculated RCS as the grid size changes. After running multiple simulations varying the grid size parameter, we found the variation in RCS due to this factor to be ±2 dB. Because the analytic distributions used to define a meteor in the simulation are not hard targets but fall off asymptotically at the edges, it is impossible to define a simulation box that
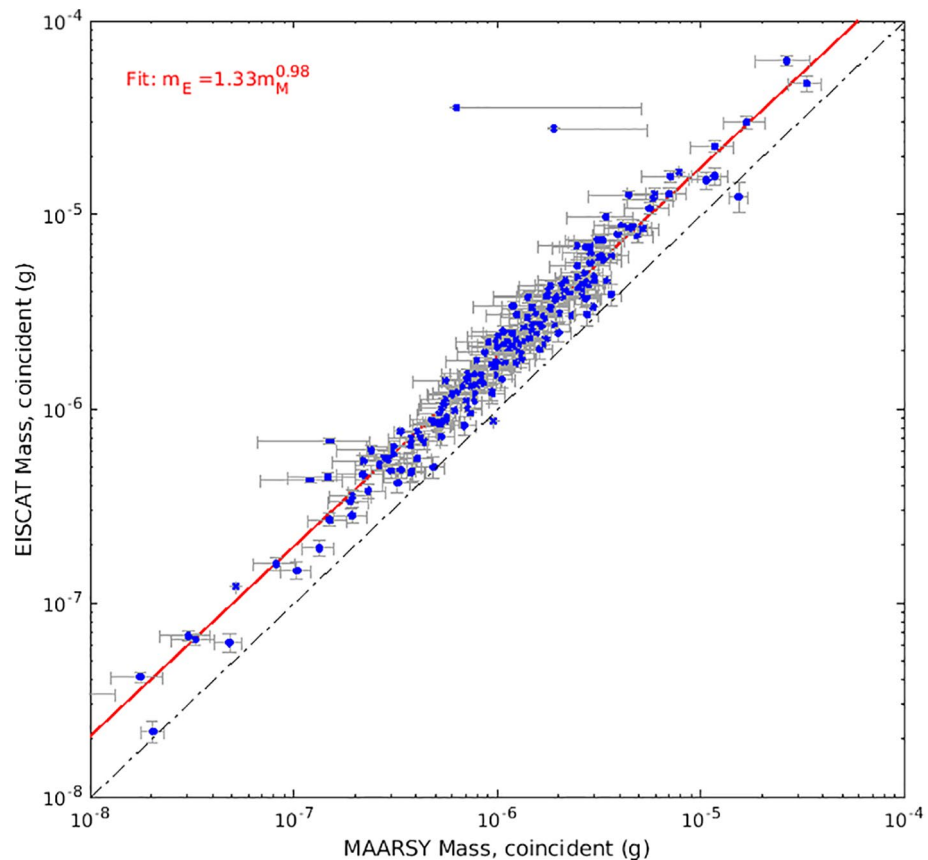
Figure 6. Masses estimated using EISCAT versus MAARSY data, with 1σ error bars. The black dashed line represents exact equality. The red line represents a linear fit in log-log space, neglecting outliers. The fit shows that there is a strong linear correlation between the two estimates, but that the EISCAT estimates are on average a factor of 1.33 greater than the MAARSY estimates.

encompasses it entirely. However, the plasma density falls off sufficiently quickly at the edges that as long as the box is "sufficiently" large (determined experimentally), there is no variation in RCS with changing box size. The linear fit used to create the lookup tables described above adds an additional RMS error of 0.4 dB. The actual error is larger in the Mie regime; however, the data set includes few meteors large enough to fall into the Mie regime (three cases, less than 0.5% of the data set). Finally, the total runtime of the simulation also causes some variation in RCS, but as long as the simulation is run long enough to capture the initial reflection of the pulse this variation is small (0.05 dB). The total error in RCS associated with all of these aspects of the FDTD model is about 2.5 dB. While other sources of error certainly exist, we believe that they are small in magnitude compared to those enumerated here. These errors are carried through the analysis and are used to calculate errors on the resulting mass distributions.

4. Results

The process described in Section 3 was applied to a set of 485 radar observations, as described in Section 2. After removing observations for which there is no coincident region or for which no mass could be determined using this method, we produce mass estimates for 271 meteors. For each individual meteor, independent mass estimates were calculated using the MAARSY and EISCAT observations, since as described above, this method requires only a single-frequency RCS measurement. Figure 6 shows a scatter plot of the EISCAT estimate plotted against the MAARSY estimate, with 1σ error bars. Note that these estimates are only of the mass produced in the coincident region. The sources and propagation of error are described in Section 3. In the coincident region, the EISCAT mass estimate is typically slightly higher than the MAARSY estimate, but there is a strong linear correlation between the two.
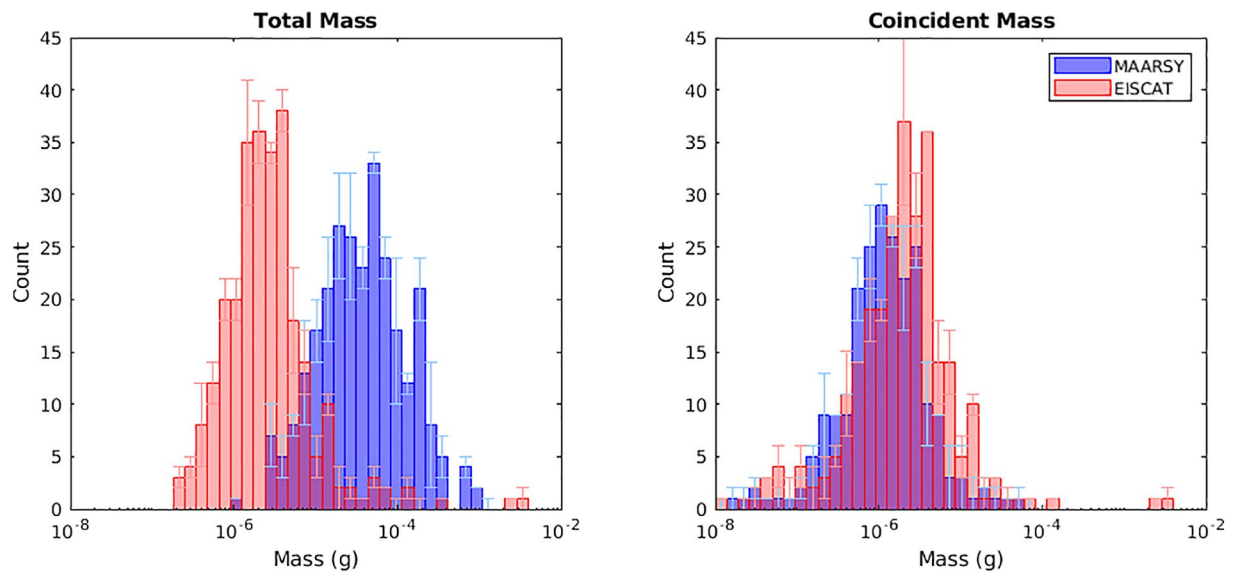
Figure 7. Mass distributions for total observations (left) and coincident observations (right), with 1σ error bars.

In general, the mass estimation scheme performs well. A linear fit in log-log space to the calculated masses (see Figure 6) shows that on average, there is a factor of 1.33 difference between the estimates, and that there is a strong linear correlation between them. However, the source of this disparity is not yet understood, as it may arise from a number of possible sources. We discuss the offset in this plot and possible sources of the discrepancy in Section 5.

The individual mass estimates can be combined to describe the mass distribution observed by both radars. The left panel in Figure 7 shows the distributions of the total meteor mass, and the right panel shows the mass lost in the coincident region. The total mass distributions show that the MAARSY distribution (median: 38 μg) peaks more than an order of magnitude higher than the EISCAT distribution (median: 2.3 μg). This result is as one might expect, given that MAARSY has a significantly larger beamwidth and observes a larger volume than EISCAT. Typically, meteors are observed for a longer duration by MAARSY due to the larger beamwidth, hence the total mass is integrated over a longer trajectory. 80% of the MAARSY masses lie between 7.7 and 192 μg; 80% of the EISCAT masses lie between 0.68 and 10 μg.

The total mass distributions are of significant scientific interest, particularly the MAARSY distribution, which captures a larger portion of the meteor trail, but they provide little insight into the validity of this method. As a validation check, we consider the coincident region masses, which include only the mass lost during the period when both radars are observing the meteor. The EISCAT and MAARSY masses are calculated using independent observations and simulations, so good agreement between them provides confidence in our inversion method. We see from Figure 6 that there is a strong linear relationship between the two estimates, with several outliers clustered at high masses. Only two of the points in Figure 6 are omitted from the fit; three more fall outside of the plot boundaries. Note that in almost all cases, the EISCAT mass estimate is greater than the MAARSY estimate. Figure 7 (right) shows the corresponding mass distributions. In this case, the EISCAT distribution peaks at slightly higher mass than the MAARSY distribution, again indicating that the EISCAT estimates are more massive than the MAARSY estimates. Possible sources for this disparity are addressed in Section 5. However, the two distributions show reasonable agreement over the whole data set.

5. Discussion and Conclusions

This paper presents a method for combining radar observations with the results of FDTD modeling to produce meteor mass estimates. Lookup tables produced from FDTD simulations relating a theoretical plasma distribution to a RCS are used to map radar observations of altitude, velocity, and RCS to line densities,

which are then integrated to estimate masses. This method enables the estimate of meteor masses from a single-frequency radar observation. The procedure is applied to 485 observed coincidentally by the EISCAT and MAARSY radars, and the masses calculated using both sets of data are compared.

While we have reduced the number of assumptions used to calculate masses where possible, some remain. In Equation 1, the ablated species mass μ and the ionization efficiency β must be specified. We have assumed a mixture of oxygen and silicon in this analysis; however, since the mass is linearly proportional to the species mass, changing the assumed μ simply scales the resulting masses. The ionization efficiency profile from DeLuca et al. (2018) is experimentally derived and is a function of velocity, rather than a constant value for all meteors. Mass is inversely proportional to the ionization efficiency, so adjusting β also linearly scales the mass. The resulting mass distributions are in reasonable agreement with past measurements. Close et al. (2004) derived masses on the order of $10^{-9} - 10^{-1}$ g using UHF and VHF radar observations and assuming Gaussian density profiles. Using the same data set as this work, (Schult et al., 2021) derived masses ranging from $10^{-7} - 10^{-2}$ g, again assuming a Gaussian distribution and using a dual-frequency technique.

The choice of where in the meteor tail to calculate the line density also introduces some variation. As shown in Figure 4b, the line density is negligible in front of the meteoroid, rises sharply and peaks at the meteoroid center, then decays slowly down the tail. Theoretically, one would expect that the line density would be constant in the tail, as the ionization produced at the meteoroid is all left in the trail, where it neither increases nor decreases. However, as the bounds of the numerical integration must be finite and the distribution approaches 0 only asymptotically, some of the density distribution lies outside of the box. The amount of particles outside the box should increase with distance from the meteoroid, as the plasma expands, which would explain the shape of Figure 4b. Further investigation has shown that doubling the box size while maintaining the size of the meteor increases the peak value of q less than 5%, indicating that most of the density is captured within the bounds of integration. In accordance with this explanation, we have chosen to calculate q just behind the meteoroid, with the goal of capturing as much of the distribution as possible.

As shown in Section 4 above, the masses estimated using EISCAT data are on average 1.33 times larger than those estimated using MAARSY data. A clue to this discrepancy is found in the difference between the MAARSY and EISCAT RCS values. Figure 8 compares the difference between the median MAARSY and EISCAT RCS for a given head echo and the expected difference based on the FDTD model. There is a wide spread in the RCS differences in the data, but on average the difference is 15–20 dB. However, the FDTD model predicts RCS differences on the order of 30 dB. The model predicts a spread of 2–3 dB in the RCS difference due to variation in altitude and velocity, but does not reproduce the more than 20 dB spread observed in the data. It is not clear whether the model is over estimating MAARSY RCS values, under estimating EISCAT RCS values, or if some of the disparity can be attributed to the RCS calculations in the radar data. Although the detection of the meteor head echoes inside the beam volume is accurate to 50–100 m (Brown et al., 2017), rapid changes in the antenna gain toward the first null introduce uncertainties in the derived SNR/RCS curves of about 3–5 dB. However, these uncertainties are not sufficient to explain the 10 dB shift. The FDTD model predicts that with increasing MAARSY RCS, a proxy for the size of the meteor, the RCS difference between the two radars decreases ($\Delta RCS \propto -0.077 \cdot RCS$); this trend is also observed in the data ($\Delta RCS \propto -0.104 \cdot RCS$). Repeating the analysis with EISCAT RCS values artificially decreased by 10 dB reduces the offset between the MAARSY and EISCAT masses from a factor of 1.33 to 1.05.

A possible source of the difference between the simulated and observed RCS differences is the aspect angle, or the angle between the radar pulse and the meteor's direction of motion. The FDTD simulations used to create the lookup tables all assume that the meteor is traveling directly toward the radar. However, the radars do not necessarily or even probably observe meteors with this viewing geometry. Due to differences in pointing direction, MAARSY observes more meteors close to head-on, while EISCAT is more likely to point close to perpendicular to the trail. Test simulations show that the RCS decreases slightly (1–2 dB) when the aspect angle is shifted by 90°, but not enough to explain the full 10 dB discrepancy. The simulations also show that EISCAT is more sensitive to aspect angle than MAARSY; rotating the meteor 90° from pointing directly at the radar to perpendicular to the beam shifts the RCS by 0.88 dB for MAARSY and 1.99 dB for EISCAT.
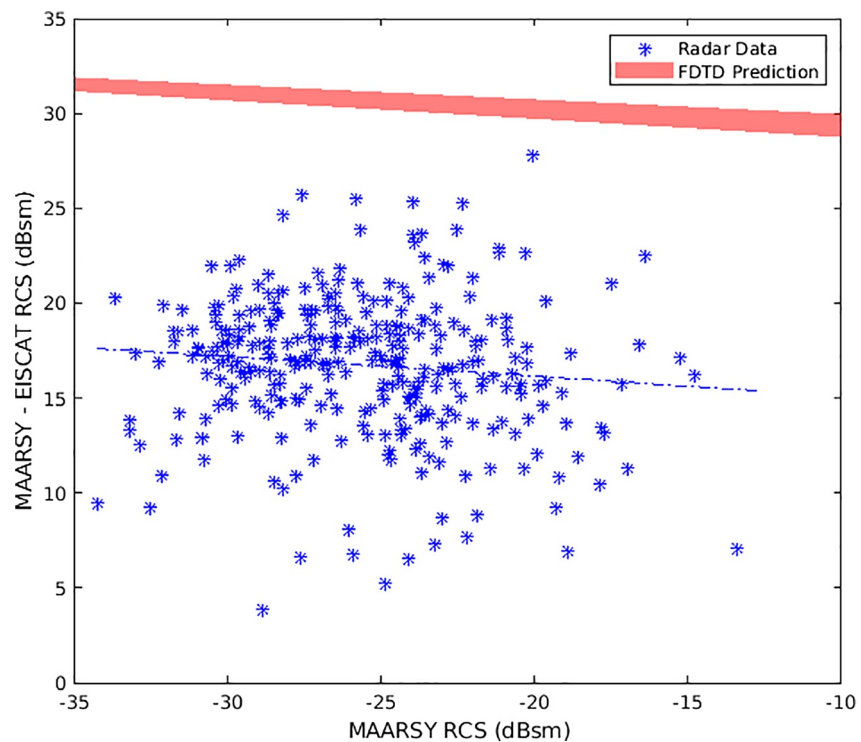
Figure 8. Radar cross section difference between MAARSY and EISCAT observations, as predicted by the finite difference time domain model (red) and in the data (blue). A linear fit to the radar data is shown by the blue dashed line.

Kero, Szasz, Wannberg, et al. (2008) used the three EISCAT UHF receivers to compare the monostatic RCS of a meteor target with two simultaneously probed bistatic RCSs at different aspect angles. Meteoroids from all possible directions entering the common volume monitored by the three receivers were detected, out to an aspect angle of 130° from the meteoroid trajectories. The RCS of individual meteors as observed by the three receivers were equal within the accuracy of the measurements, which is consistent with an essentially isotropic scattering process as had previously been inferred from polarization measurements by Close et al. (2002). The results of the simulations presented here indicate that aspect angle might play a more significant role than previously thought, particularly when comparing observations from radar of different frequencies. We intend to investigate the importance of the aspect angle in future work, as well as the effects of fragmentation. Fragmentation has been shown to occur in a substantial number of meteors, and can have a substantial effect on mass estimates (Babadzhanov, 2002; Campbell-Brown & Jones, 2003). In the case of this analysis, small (nm-scale) particles that fragment from the main body of the meteoroid might increase the apparent size seen by EISCAT, while not significantly affecting the MAARSY observation. By overlapping two or more iterations of the DO distribution, we can take the first steps toward modeling fragmented meteors using the FDTD code.

As discussed in Section 3.3, we have propagated all sources of error that we could constrain in this analysis. On the modeling side, these include variation in the grid size, the box size, and the total duration of the simulation. Where possible, model parameters were chosen to minimize these errors. We also include error due to the interpolation and fitting involved in the process of determining the size parameter. When propagated through the analysis, the resulting mass error due to FDTD simulation errors is in general about 10%. We do not include uncertainties in the radar measurements in this analysis.

The ultimate goal of developing this method is to apply it broadly in order to estimate the total mass flux and mass distribution entering the Earth's atmosphere. While dual frequency measurements are required for the verification and comparison performed in this work, the general method requires only a single frequency. It can thus be used on datasets from many radar systems at various frequencies, although modeling

constraints currently restrict the FDTD simulations to frequencies less than 1 GHz. However, this limitation is due to constraints on computer resources used by the FDTD simulations, and could be overcome by increasing the parallelization of the FDTD code or improved computing power.

Data Availability Statement

The FDTD lookup tables and processing code used in this analysis are available on Zenodo at http://doi.org/10.5281/zenodo.4723667. The radar data is available on Zenodo at http://doi.org/10.5281/zenodo.4731084.

References

Babadzhanov, P. (2002). Fragmentation and densities of meteoroids. *A&A*, *384*(1), 317–321. https://doi.org/10.1051/0004-6361:20020010

Brown, P., Stober, G., Schult, C., Krzeminski, Z., Cooke, W., & Chau, J. (2017). Simultaneous optical and meteor head echo measurements using the middle atmosphere alomar radar system (maarsy): Data collection and preliminary analysis. *Planetary and Space Science*, *141*, 25–34. https://doi.org/10.1016/j.pss.2017.04.013

Campbell-Brown, M., & Jones, J. (2003). Determining the initial radius of meteor trains: Fragmentation. *Monthly Notices of the Royal Astronomical Society*, *343*(3), 775–780. https://doi.org/10.1046/j.1365-8711.2003.06713.x

Ceplecha, Z., Borovička, J., Elford, W., ReVelle, D. O., Hawkes, R. L., Porubčan, V., & Šimek, M. (1998). Meteor phenomena and bodies. *Space Science Reviews*, *84*, 327–471. https://doi.org/10.1023/A:1005069928850

Close, S., Oppenheim, M., Hunt, S., & Coster, A. (2004). A technique for calculating meteor plasma density and meteoroid mass from radar head echo scattering. *Icarus*, *168*(1), 43–52. https://doi.org/10.1016/j.icarus.2003.11.018

Close, S., Oppenheim, M., Hunt, S., & Dyrud, L. (2002). Scattering characteristics of high-resolution meteor head echoes detected at multiple frequencies. *Journal of Geophysical Research*, *107*(A10), SIA 9-1-SIA 9-12. https://doi.org/10.1029/2002JA009253

DeLuca, M., Munsat, T., Thomas, E., & Sternovsky, Z. (2018). The ionization efficiency of aluminum and iron at meteoric velocities. *Planetary and Space Science*. (Dust, Atmosphere, and Plasma Environment of the Moon and Small Bodies), *156*, 111–116. https://doi.org/10.1016/j.pss.2017.11.003

Dimant, Y. S., & Oppenheim, M. M. (2017). Formation of plasma around a small meteoroid: 2. Implications for radar head echo. *Journal of Geophysical Research: Space Physics*, *122*, 4697–4711. https://doi.org/10.1002/2017JA023963

Elford, W. G., Cervera, M. A., & Steel, D. I. (1995). Meteor velocities: A new look at an old problem. *Earth Moon and Planets*, *68*(1-3), 257–266. https://doi.org/10.1007/BF00671514

Ellyett, C., & Kennewell, J. (1980). Radar meteor rates and atmospheric density changes. *Nature*, *287*, 521–522. https://doi.org/10.1038/287521a0

Flynn, G. J. (2002). Extraterrestrial dust. In E. Murad, & I. P. Williams (Eds.), *Meteors in the earth's atmosphere*. Cambridge. Cambridge University Press.

Hunt, S., Oppenheim, M., Close, S., Brown, P., McKeen, F., & Minardi, M. (2004). Determination of the meteoroid velocity distribution at the earth using high-gain radar. *Icarus*, *168*(1), 34–42. https://doi.org/10.1016/j.icarus.2003.08.006

Inan, U. S., & Marshall, R. A. (2011). *Numerical electromagnetics: The fdtd method*. Cambridge University Press. https://doi.org/10.1017/CBO9780511921353

Janches, D., Plane, J. M. C., Nesvorný, D., Feng, W., Vokrouhlický, D., & Nicolls, M. J. (2014). Radar detectability studies of slow and small zodiacal dust cloud particles. I. The case of Arecibo 430 MHz meteor head echo observations. *Astrophysical Journal*, *796*(1), 41. https://doi.org/10.1088/0004-637X/796/1/41

Janches, D., Swarnalingam, N., Plane, J. M. C., Nesvorný, D., Feng, W., Vokrouhlický, D., & Nicolls, M. J. (2015). Radar Detectability studies of slow and small zodiacal dust cloud particles: II. A study of three radars with different sensitivity. *Astrophysical Journal*, *807*(1), 13. https://doi.org/10.1088/0004-637X/807/1/13

Kero, J., Szasz, C., Nakamura, T., Meisel, D. D., Ueda, M., Fujiwara, Y., et al. (2012). The 2009–2010 MU radar head echo observation programme for sporadic and shower meteors: Radiant densities and diurnal rates. *Monthly Notices of the Royal Astronomical Society*, *425*(1), 135–146. https://doi.org/10.1111/j.1365-2966.2012.21407.x

Kero, J., Szasz, C., Pellinen-Wannberg, A., Wannberg, G., Westman, A., & Meisel, D. D. (2008). Determination of meteoroid physical properties from tristatic radar observations. *Annales Geophysicae*, *26*(8), 2217–2228. https://doi.org/10.5194/angeo-26-2217-2008

Kero, J., Szasz, C., Wannberg, G., Pellinen-Wannberg, A., & Westman, A. (2008). On the meteoric head echo radar cross section angular dependence. *Geophysical Research Letters*, *35*, L07101. https://doi.org/10.1029/2008GL033402

Love, S. G., & Brownlee, D. E. (1993). A direct measurement of the terrestrial mass accretion rate of cosmic dust. *Science*, *262*(5133), 550–553. https://doi.org/10.1126/science.262.5133.550

Marshall, R. A., & Close, S. (2015). An fdtd model of scattering from meteor head plasma. *Journal of Geophysical Research: Space Physics*, *120*, 5931–5942. https://doi.org/10.1002/2015JA021238

Mazur, M., Pokorný, P., Brown, P., Weryk, R. J., Vida, D., Schult, C., et al. (2020). Precision measurements of radar transverse scattering speeds from meteor phase characteristics. *Radio Science*, *55*(10), e2019RS006987. https://doi.org/10.1029/2019RS006987

McKinley, D. W. R., & Millman, P. M. (1949). A phenomenological theory of radar echoes from meteors. *Proceedings of the IRE*, *37*(4), 364–375. https://doi.org/10.1109/JRPROC.1949.231641

Plane, J. (1991). The chemistry of meteoric metals in the earth's upper atmosphere. *International Reviews in Physical Chemistry*, *10*, 55–106. https://doi.org/10.1080/01442359109353254

Plane, J. (2012). Cosmic dust in the earth's atmosphere. *Chemical Society Reviews*, *41*, 6507–6518. https://doi.org/10.1039/C2CS35132C

ReVelle, D. O. (2003). Meteors in the earth's atmosphere: Meteoroids and cosmic dust and their interactions with the earth's upper atmosphere. *Eos, Transactions American Geophysical Union*, *84*(26), 249. https://doi.org/10.1029/2003EO260012

Rosinski, J., & Pierrard, J. (1964). Condensation products of meteor vapors and their connection with noctilucent clouds and rainfall anomalies. *Journal of Atmospheric and Terrestrial Physics*, *26*(1), 51–66. https://doi.org/10.1016/0021-9169(64)90108-4

Schult, C., Kero, J., Stober, G., & Brown, P. (2021). Dual frequency measurements of meteor head echoes simultaneously detected with the maarsy and eiscat radar systems. *Icarus*, *355*, 114137. https://doi.org/10.1016/j.icarus.2020.114137

Schult, C., Stober, G., Brown, P., Pokorný, P., & Campbell-Brown, M. (2020). Characteristics of very faint (+16) meteors detected with the middle atmosphere alomar radar system (maarsy). *Icarus*, *340*, 113444. https://doi.org/10.1016/j.icarus.2019.113444

Schult, C., Stober, G., Janches, D., & Chau, J. L. (2017). Results of the first continuous meteor head echo survey at polar latitudes. *Icarus*, *297*, 1–13. https://doi.org/10.1016/j.icarus.2017.06.019

Steel, D., & Elford, W. (1991). The height distribution of radio meteors: Comparison of observations at different frequencies on the basis of standard echo theory. *Journal of Atmospheric and Terrestrial Physics*, *53*(5), 409–417. https://doi.org/10.1016/0021-9169(91)90035-6

Stober, G., Jacobi, C., & Singer, W. (2011). Meteoroid mass determination from underdense trails. *Journal of Atmospheric and Solar-Terrestrial Physics*. (Scientific Results from Networked and Multi-instrument studies based on MST Radar), *73*(9), 895–900. https://doi.org/10.1016/j.jastp.2010.06.009

Yee, K. S. (1966). Numerical solution of initial boundary value problems involving Maxwell's equations in isotropic media. *IEEE Trans. Antennas and Propagation*, *14*, 302–307. https://doi.org/10.1109/tap.1966.1138693